Int J Fract
https://doi.org/10.1007/s10704-024-00815-1

RESEARCH

Crack propagation behavior in the stacked *TaC–Gr* core–shell composites

Asghar Aryanfar · Mert Kulak · Nasser P. Vafa · Vahideh Shahedifar · Mahdi G. Kakroudi

Received: 2 December 2023 / Accepted: 1 September 2024

Abstract The catastrophic fracture of the ceramics limits their utilization in industrial applications. Particularly despite the wide potential of the Tantalum carbide (TaC) it is prone to sudden fracture due to its brittleness. Therefore, covering it with the ductile graphite (Gr) shell could improve its toughness as a shock absorber. In this regard, a percolation-based image processing framework is developed to quantify the area, periphery, and tortuosity of the generated cracks, as a measure for the crack deflection, from three distinct methods and correlate it to the shell fraction, stacking mode, and the fracture energy. As well, defining equivalent material for the core–shell composition, finite element simulations were carried out to project the local (i.e. real state) shape function versus the crack progress which has led to the estimation of the critical crack size in flexural leading. The results are useful for quantifying and optimization of the design parameters for the core–shell composites and their arrangements versus the specified application.

Supplementary Information The online version contains supplementary material available at https://doi.org/10.1007/s10704-024-00815-1.

A. Aryanfar (✉) · M. Kulak
Boğaziçi University, Bebek, 34342 Istanbul, Turkey
e-mail: aryanfar@caltech.edu

N. P. Vafa · M. G. Kakroudi
University of Tabriz, 29 Bahman Blvd, Tabriz, Iran

V. Shahedifar
Urmia University, 11 Sero Road, Urmia, Iran

Keywords Tortuosity · Fibre ceramics · Composites · Stacking · Fracture

List of symbols

l	Loading span/ domain width (m)
h	Sample height (m)
d	Sample depth (m)
a	Notch depth (m)
a_C	Critical notch depth (m)
E_C	Modulus of elasticity of core (Pa)
E_S	Modulus of elasticity of shell (Pa)
E_{EFF}	Effective elastic modulus of the composite (N m^{-2})
G_{EFF}	Effective shear modulus of the composite (N m^{-2})
α	Graphite shell fraction
S_{yC}	Yield strength of TaC (Pa)
S_{yS}	Yield strength of graphite (Pa)
F	Applied flexural force (N)
S_y	Yield strength of the composite (Pa)
E_{Main}	Energy absorbed by main branch (J m^{-1})
E_{Branch}	Energy absorbed by (sub-)branches (J m^{-1})
δ	Displacement under the applied force (μm)
K_{IC}	Fracture toughness ($\text{Pa}\sqrt{\text{m}}$)
E_{TOT}	Total applied energy (J m^{-1})

Published online: 30 September 2024

E_{EL}	Elastic Energy ($J\,m^{-1}$)
E_{FR}	Fracture Energy ($J\,m^{-1}$)
K_{THE}, K_{SIM}, K_{EXP}	Theoretical, simulation and experimental stiffness of composite material ($N\,m^{-1}$)
τ	Crack tortuosity ([ ])
ν_{EFF}	Effective poisson ratio of the composite ([ ])

1 Introduction

Ceramics are widely used in the industry as heat and corrosion-resistant components (Heimann 2010; Temple and Ronald 2020). However, their brittle behavior makes them prone to fracture, particularly when exposed to a high temperature and large loads (Deng et al. 2017; Liu et al. 2016), limiting their extensive applications. As a sub-group, carbides possess extremely high-temperature resistance during refractory use, and particularly tantalum carbide (TaC), has excellent mechanical properties, far exceeding the best polycrystalline graphite (Nino et al. 2015; Yasmin and Daniel 2004). Its high melting point ($> 3880\,°C$) makes it the only material with acceptable resistance in the temperature range of 2900 °C to 3200 °C and it has remarkable hardness, elastic modulus, and chemical inertness (Linstrom and Mallard 2001; William et al. 2014; Rezaei et al. 2017).

Additionally, tantalum carbide TaC is used in cutting tools to increase the substrate metal resistance to chemical corrosion and wear via hard coating. It serves as a blade material in the jet engine turbines and rocket nozzle coating, which can improve erosion resistance and prolong the respective service life significantly. Because of the good conductivity, tantalum carbide can be used as electrode material, and can also turn to complex shapes via wire cutting. At atomic level, its notable physical and chemical properties could be attributed to the mixed covalent-metallic bond (Torre et al. 2005). However, the shortcoming is the extreme sensitivity to thermal shock, where the containing carbides possess low thermal conductivity and high thermal expansion coefficient, preventing their application as aerospace materials. Nevertheless, the competition between the strength and toughness of TaC composited with fiber, platelet, or particle inclusions (Silvestroni et al. 2015) requires greater effort to improve its resistance to fracture, while maintaining superior properties in application at extreme conditions.

Hence, the proper choice of material combinations and fabrication methods boosts materials' resistance to tragic failure by forcing the fracture to perform more work while creating abundantly new free surfaces. In this regard, the formation of the cracks is a significant indicator, particularly during the instigation stage. Internal stresses in the structure are created by effects such as cyclic loading and fatigue stress, which can lead to fracture. In fact, a close look reveals that ductile crack growth precedes the fracture, which is predicted by the ductile damage model (Moattari et al. 2016). The crack typically propagates along the weak cell boundaries and absorbs a high amount of energy (Bermejo and Danzer 2010). The occurrence of crack tip blunting at material interfaces is followed by significant instances of delamination depending on the elastic mismatch strain from the residual stress and the difference in the coefficient of thermal expansion of the compartments (Warwick and Clegg 2009). As an example, in ceramic matrix composites, the crack onset location is governed by the grain's shape, but its direction of propagation depends on the fiber orientation (Luna et al. 2020).

A Myriad of techniques has been proposed to address or circumvent the brittleness problem (Bai et al. 2018). Brittle-ductile multi-layered steel composites have been investigated by reducing the thickness of the layers, and two extreme conditions of tunnel cracking (elasticity and shear lag limit) are identified, as the upper and lower bounds of the observed transition (Inoue et al. 2008). The explored methods and materials are thickness, volume fraction and orientation of laminates (Adharapurapu et al. 2005) and their toughness (Hwang et al. 2001), the type of inter-material or inter-laminar bonding (Bai et al. 2019; Davis et al. 2000; Hilmas et al. 1995; Li et al. 2008; Zou et al. 2003; Bueno and Baudín 2009) for absorbing the energy, crack deflection and maintaining the structural integrity.

Additional works include ballistic loading (Boccaccini et al. 2005), microstructure effect(Li and Zhou 2013), solidified ceramics (Perrière et al. 2008), grain size (Bower and Ortiz 1993), patterned inclusion (Wei et al. 2019), bi-material multilayered media (Muju 2000) and estimating effective toughness in heterogeneous media (Hossain et al. 2014). The crack behavior during the fracture has been investigated from the point

of penetration, deflection by including a tougher layer (Liu and Hsu 1996), delamination (Phillipps et al. 1993; Clegg et al. 1994; Watts and Hilmas 2006; Faber et al. 1983), bridging (Bower and Ortiz 1991; Hvizdoš et al. 2013), and bifurcation (Khan 2019; Wei et al. 2014; Oechsner et al. 1996). Particularly, crack deflection versus crack penetration has been compared via simultaneous consideration of the fracture toughness and the strength (Parmigiani and Thouless 2006). Moreover, one of the prominent methods of controlling such failure has been coating the ceramic with more ductile materials to improve their toughness during the fracture (Baskaran and Halloran 1993; Kovar et al. 1997).

Modeling-wise, the applicability of ceramic laminates have been explored, which divide the tough and brittle interfaces (Valerio Carollo and Reinoso 2018). The branching pattern of the cracks is explored versus the interface coherence, where in extreme cases they are either perfectly bonded or fully separated (Dusane et al. 2022). Meanwhile, the formulation of the fracture criterion has been developed for non-linear visco-elastic solids in non-local form and rate form-based finite deformation, which uses the averaged Gibbs potential as the damage measure and eliminates mesh-type dependency on the neighborhood of the crack tip as the singularity node (Thamburaja et al. 2019; Sarah et al. 2020). Additionally, the earlier works have explored the mesh dependency on the brittle fracture via the inclusion of cohesive elements with Weibull distribution, where the larger elements are more likely to contain defects (Zhou and Molinari 2004). The anisotropic and isotropic meshing patterns have been developed separately for the crack neighborhood and its far-field respectively (Artina et al. 2015). As well, the dynamic crack growth has been investigated via the moving mesh method (Fabbrocino et al. 2019) as well as a comparison of the blunt and sharp cracks (Needleman and Tvergaard 1994) and the mesh bias has been explored in the context of analogy between the embedded crack versus smeared crack models (Mosler and Meschke 2004).

One of the experimental methods for investigating the cracks is forced tearing. In this regard, a single oscillatory crack arises when a tool is driven laterally through a brittle sheet, while two diverging cracks and a series of concertina-like folds form when a tool is forced laterally through a ductile sheet (Tallinen and Mahadevan 2011). The crack pattern of thin elastic bodies, including the diverging concertina tearing, the perforation of a thin sheet by a cone and the star shape pattern of impacted windows are ruled by a balance between stored elastic energy and surface creation energy in the soft brittle bodies (Vandenberghe and Villermaux 2013). The benefit may be taken from statistical size effects, which are strongly dependent on the crack geometry. Experimental fatigue and ductile tearing studies show similar development of complex cracks towards the re-characterized shape and procedures (Boštjan et al. 2003).

Regarding the characterization of the post-fracture cracks several image-processing approaches have been proposed. The primary benefit of image-based fracture detection over traditional manual approaches is the higher precision,[1] managing insufficient information, and vast flexibility in capturing the structure of an object (Entezari et al. 2016; Hefter et al. 1993; Lee et al. 2016).

In this paper, we develop a new image processing framework for quantifying the cracking behavior of TaC based on the fibre content and the alignment of the sub-components. The crack tortuosity has been explored as a measure of resistance to the fracture. In this regard, distinct methods have been used to compute the crack pathways and the degree of twisted-ness. The methods have been analyzed against each other, for explaining the role of laminate arrangements as well as the fraction of the ductile shell. The results could be useful for designing the space of parameters in the trade-off between the brittle-ness and ductile-ness for the given specified application.

2 Experimental

Figure 1a shows the schematic of the 3-point experimental setup where the increase in the central flexural loading ultimately leads to the fracture in the center. The sample medium consists of composite core–shell which are illustrated in the Fig. 1b and vary in terms of the arrangement of core–shell co-extrudes (perpendicular vs parallel) and their respective shell compositional fractions (α). Regarding the core, tantalum carbide TaC (Hunan Haiyun Metallurgical Materials Co., Ltd., China) powders were purchased and prepared with the mixture of 75% (vol) and TaC and 20% Hafnium carbide Hfc where initially 5% powder was dissipated

[1] Particularly via high-resolution cameras.

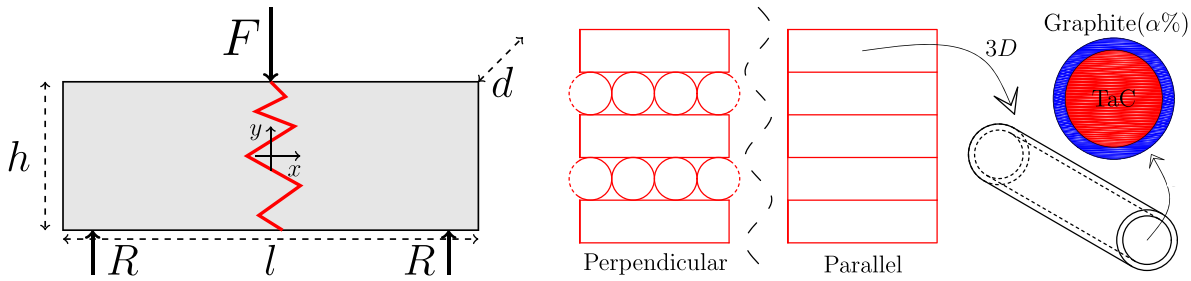

Fig. 1 Schematics of the **a** experimental setup and **b** stacking-mode/compositions. **a** Experimental Setup. The flexural load F is applied in the top center of the composite beam of length, height and depth dimensions $l \times h \times d$ with two support reactions R, causing the schematically shown crack in red. **a** The two stacking modes of Perpendicular (0–90, left) and Parallel (0–0, center) for the beams which consists of core (C) and shell (S) compartments with the volumetric fraction of $(1-\alpha)$ and α respectively

for 15 min in a 265W ultrasonic agitator using ethanol for immersion. Subsequently, the HfC and TaC powders were gradually poured into the slurry and were mixed for 30 min, which was ball-mixed for another 60 min in a polyethylene cup. Afterward, the homogeneous slurry was dried at 100 °C by a rotary hot plate to minimize segregation and then sieved via a 60-mesh screen. For co-extrusion 0.16% (wt) polyvinyl alcohol (PVA) together with 0.16% (wt) Carboxymethyl cellulose (CMC) were employed as polymer binders, while 0.5% (wt) glycerol was used as a plasticizer.

Afterwards, the ceramic particles were mixed with a liquid mixture of organic components in a high-shear mixer for 5 min. Then, it was extruded into a $\sim$ 10 mm diameter rod. Furthermore, the graphite powder consisting of flake particles 20−30 μm in diameter and 0.5 μm in thickness was applied to the shell material. After mixing graphite powder with binders including 1.4% (wt) PVA and 0.3% (wt) CMC, a cylindrical shell with a $\sim$ 10 mm inner diameter was extruded similarly. While the thickness of the cylindrical shells varied for the specimens, the core was inserted and co-extruded to create $\sim$ 1 mm diameter fibers.

The green billets were prepared by aligning the fibers at 0° and 90° relative to the x axis in a steel mold of 25 × 10 mm^2 and cold-pressed with 30 MPa. The billets were inserted into a graphite die with four rectangular holes of the same area, covered with boron nitride and lined with a flexible graphite foil. After binder burnout between 250 and 550 °C with a low heating rate of 5 °C min^{-1} in the vacuum atmosphere (0.05 Pa), the sintering process was carried out at 1800 °C with the pressure of 40 MPa for 1 h by a resistance-heated hot press furnace (Shenyang Weitai Science & Technology Development Co., China). Based on the thermogravimetric analysis (TGA), the polymer binders were decomposed at the initial temperatures of the sintering process, and the gasses from degradation were removed by the vacuum of the hot press chamber (Vahideha and Mahdi 2018; Rezaei et al. 2017; Shahedifar et al. 2020).

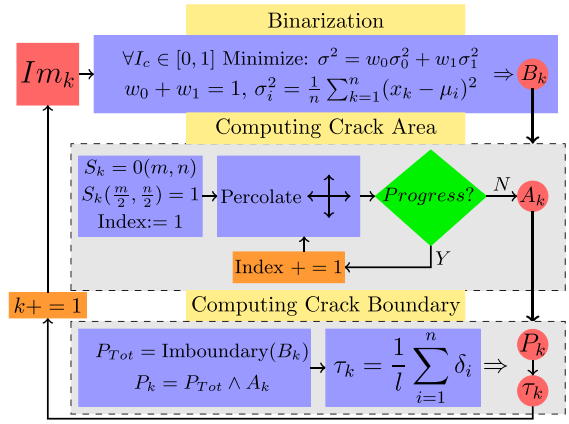

Fig. 2 Pseudo-chart for the image processing and computing each crack area A_k and total periphery P_{Tot}, which leads to extracting the crack periphery P_{k} (left and right) and it's respective tortuosity τ

The shell volume ratio α was defined as:

$$\alpha = \frac{A_S}{A_C + A_S} \tag{1}$$

where A_C and A_s are the cross-sectional areas of the core and shell respectively. The specimens were made in three different shell volume ratios ($\alpha = \{25, 30, 35\}$) and two stacking modes of parallel and perpendicular arrangements (0–0 and 0–90)which were hot pressed at 1800 °C. The resulting core–shell structures were utilized in the flexural load test until the cracks formed.

Table 1 The parameters of the experimental setup. l: length, h: height, d: depth, E, G: elastic and shear modulus, ν: Poisson ratio. The subscripts C and S represent the core and shell respectively

Parameter	$l \times h \times d$	E_C, E_S	$\sigma_{y,C}, \sigma_{y,S}$	G_C, G_S	ν_C, ν_S
Value	$25 \times 10 \times 15$	560, 30.8	1200, 40.4	220, 12.3	0.24, 0.3
Unit	mm^3	GPa	MPa	MPa	[ ]
Ref.	Assigned	(Nino et al. 2015; William et al. 2014), Azom[a]	(Peng et al. 2017), Azom[b]	MatWeb [c], [3]	[5], [3]

[a]https://www.azom.com/properties.aspx?ArticleID=1630
[b]https://www.azom.com/properties.aspx?ArticleID=516
[c]https://www.matweb.com/search/datasheet.aspx?matguid=9b8f8c69fe92446491de3c3dff2ef3e6&ckck=1

Table 1 provides the physical and mechanical properties of the samples.

3 Tortuosity Modeling

Figure 2 shows a simplified pseudo-chart of the steps to extract the geometrical properties of the cracks from the experimental images. The procedure is as follows:

1. Binarization (B_k): The bare image Im_k from the fractured composite contains information from the red, green, and blue values (i.e. $\{R, G, B\} \in [0, 255]$) which can be transferred to a normalized gray-scale intensity image by the following fractions respectively (Qiu et al. 2008):

$$f = \begin{bmatrix} 0.299 & 0.587 & 0.114 \end{bmatrix} \tag{2}$$

where the $0 \leq I_{i,j} \leq 1$ is the intensity value of the obtained grayscale image, a sample of which is shown in the Fig. 3a. The composite regions can be distinguished by establishing a grayness threshold, $I_c \in [0, 1]$, which classifies the elements into black and white classes $\{B, W\} \in (0, 1)$. This value is determined iteratively from Otsu's method by minimizing the intra-class variance σ^2 as follows (Otsu 1975; Asghar et al. 2019):

minimize σ^2 such that:

$$\begin{cases} \sigma^2 = \omega_0 \sigma_0^2 + \omega_1 \sigma_1^2 \\ \omega_0 + \omega_1 = 1 \end{cases} \tag{3}$$

where ω_0 and ω_1 are the fractions of black/white portions and σ_0^2 and σ_1^2 are the corresponding variances for each classified zone. The obtained binarized image from the minimization of intra-class variance σ^2 quarantines the closest proximity in the values of each chosen group ($B\&W$). Therefore, it ensures the best approximation of the original gray-scale image.

2. Crack Periphery (P_{Crack}): The total boundary of black and white regions P_{Tot} can be obtained by locating the zones between 0 and 1 identified zones as shown in Fig. 3b. Alternatively, such border could get identified via the locus of sharp changes in the color intensity.

3. Crack Area (A_{Crack}): Manually locate the top center position of each crack as the initiation point, and propagate through the first-order neighbors (i.e. left $\leftarrow$, right $\rightarrow$, top $\uparrow$, bottom $\downarrow$) (Asghar et al. 2019; Dijkstra 1959). Moving forward each new pixel is indexed in descending order. Hence, the last reaching point (i.e. edge) will contain the index of 1 and moving through the neighbors toward the starting point, the index will be increased. In fact, the magnitude of the index for a given pixel illustrates how far it is from the end point of the percolation run. As a result, the starting point will have the maximum index value, the larger index will be older (reached at earlier) and the smaller index will be younger (reached at later) in the propagation steps.

Continue the propagation until no additional progress is possible and the boundary of the crack is reached. In other words, initiating from a point inside the crack, and moving through 1st order neighbors, the percolating cluster will keep growing, as long as it propagates within the internal zones of the crack (recognized as 1), until reaching the border of the crack. However, beyond the border zones the elements (pixels) are recognized as 0 and and hence the growing cluster will not propagates further. Such percolation captures the detailed shape and area of the crack in the pixel level.

Therefore, the crack area A_{Crack} is obtained precisely. Figure 3c illustrates a sample of such percolation (color-indexed) through the formed crack.

4. Convex Hull: In order to reduce the computational cost, first we create a convex hull region of the crack Polyshape structure, as shown in the Fig. 4a, with

no self-intersection, meaning that no line segment connecting two locations on the edges ever passes outside the polygon (Jayaram and Fleyeh 2016).

5. Crack Periphery: The periphery of the crack P_{Crack} is obtained via the intersection of the sample boundary P_{Tot} and the crack area A_{Crack} as below:

$$P_{\text{Crack}} = A_{\text{Crack}} \wedge P_{\text{Tot}} \tag{4}$$

The sample of crack periphery P_{Crack} is illustrated in the Fig. 4b (in green).

6. Tortuosity: The twisted-ness (zigzag behavior) of each crack is the measure for the resistivity for the crack propagation as the sign of crack deflection. Hence, for a given segmented line of several infinitesimal length's δs_k, consisting of n points, the tortuosity τ is computed as follows:

$$\tau = \frac{\int ds}{L} = \frac{\sum_{k=1}^{n-1}\sqrt{\delta x_k^2 + \delta y_k^2}}{\sqrt{\left(\sum_{k=1}^{n-1}\delta x_k\right)^2 + \left(\sum_{k=1}^{n-1}\delta y_k\right)^2}} \tag{5}$$

where the δx_k and δy_k are the respective horizontal and vertical projection of the element δs_k and L is the length of the straight connecting the two ends.

Three distinct methods have been used to compute the form of each crack, explained as below:

6.1 Dijkstra's shortest path (S):

The shortest path algorithm, which was originally developed by Skiena (1990), was extracted as below:

i. Forward percolation: Starting from the top interface, percolate forward from the 1st order neighbors (i.e. top ↑, bottom ↓, left ←, right →) and index each new addition in descending order. Hence, the initial points will have the maximum index (i.e. equal to the largest step of propagation), and the final points will end of in the index of 1.

ii. Backward Percolation: The largest index in the bottom interface ($y = H$) indicates that the crack has reached that location at the earliest, and should be considered for the initiation of the shortest path. Therefore, starting from that element, we revert backward from the 1st order neighbors by ascending order of indexes (i.e. for index k the previous connection point would be index $k + 1$) until reaching back to the top interface ($y = 0$). The extracted path is the shortest distance between the top and bottom surface, which is indicated by the red line in the Fig. 4c. For the pathways of the same beginning/end (i.e. same length) one of them is eliminated in favor of the other.

6.2 Mid-section pathway (M):

The mid-section crack pathway is identified as the median point of each row in the crack between the left and right boundaries. Therefore, connecting the points will approximate the crack pathway, affected by the width of each section.

6.3 Averaged Left-Right (LR):

For this method, the individual tortuosities of the left and right boundaries (shown by the dashed pink-green lines in the Fig. 4c) are calculated from the Eq. (5) and has been averaged tortuosity τ of the pathways is tracked from the left and right periphery of the crack and ultimately gets averaged.

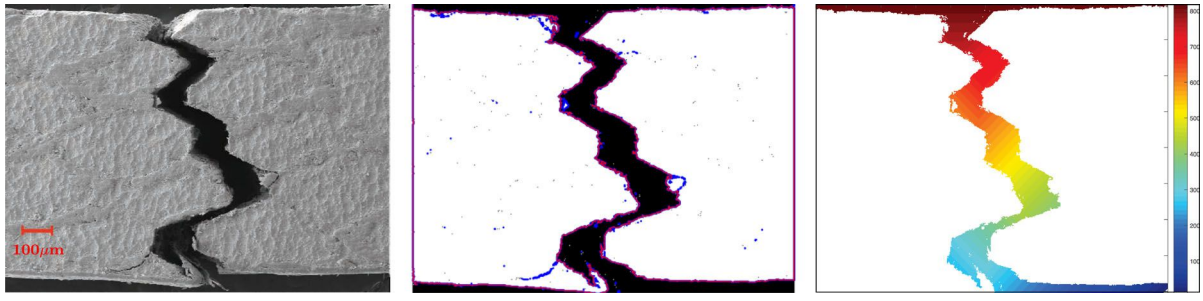

(a) Experimental crack sample after the full fracture.

(b) Captured periphery P_{Tot} from the binarized image (purple).

(c) Obtained crack area A_{Crack} using percolation through the 1^{st} order neighbors.

Fig. 3 Image processing procedure for the extracting the domain boundaries and their respective filling areas. For (**c**) the colorbar represents the index of the percolation through the inner walls of the crack which is the maximum ($\approx 800s$) for the starting point (i.e. center top) and minimum ($= 1$) for the end point (i.e. center bottom)

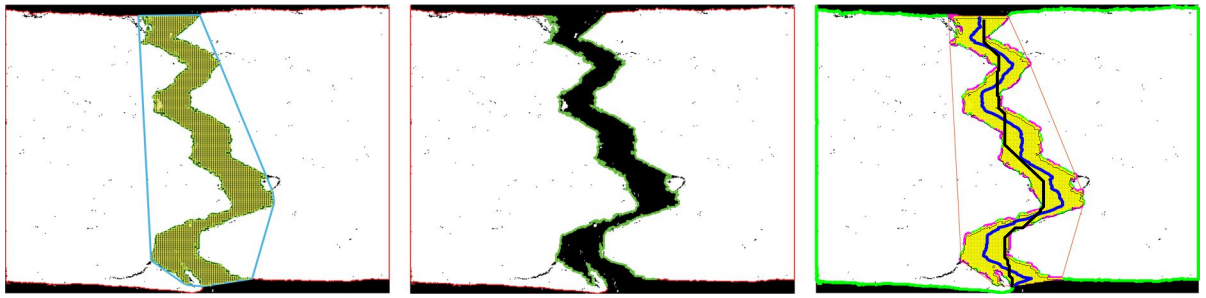

(a) Locating the convex hull surrounding the crack (light blue) for reducing the total periphery and the computational cost. The top and point of the hull were identified by a sharp slope change from ∼horizontal to ∼vertical direction of movement in the neighbors of the domain periphery P_{Tot}.

(b) Obtained crack periphery P_{Crack} (green) from the confluence of image periphery P_{Tot} and the crack area A_{Crack}.

(c) Three methods of computing the tortuosity τ for the crack. Red: Dijskstra's shortest path (S), blue: midsection (M) ; dashed pink: Left/Right boundary averaging (LR).

Fig. 4 Procedure for percolation-based extraction of crack tortuosities τ

Additionally, the applied force F versus the obtained displacement δ diagrams versus the stacking mode as well as the core–shell compositions are obtained and analyzed in the results and discussions.

4 Simulations

In order to understand the underlying mechanism leading to the rate of crack propagation, a series of simulations have been carried out using ABAQUS finite element simulation software. In this regard, the central zone during the flexural bending carries the highest moment and hence becomes the most critical. As well, the shear stress in the central cross-section should be simultaneously both opposite (action–reaction) and equal due to symmetry. Hence it will vanish ($\tau_{\text{Center}} = 0$). Therefore, the crack opening in the center is mainly caused by the remaining horizontal stresses (σ_x) from the imposed moment, and the analysis are simplified into one-dimensional exploration of stress and strain in the horizontal direction (i.e. $\square_x$). As well, the assigned equivalent material has the effective mechanical property $\square_{EFF}$, as a function of both core $\square_C$ and shell $\square_S$ mechanical properties, which is described in the next section. In this regard, the effective stress $\sigma_{EFF,x}$ in the central cross-section (mid-way between the left/right ends) is assumed to be linear elastic, perfectly plastic as below:

$$\sigma_{EFF,x} = \begin{cases} E_{EFF}\epsilon_x & \epsilon_x \leq \epsilon_{y,EFF} \\ \sigma_{y,EFF} & \epsilon_x > \epsilon_{y,EFF} \end{cases}$$

where E_{EFF} is the effective elastic modulus, ϵ_x is the resulted horizontal strain in the center, $\epsilon_{y,EFF}$ is the effective yield strain. Due to the change of the governing equations during the pre-crack and post-crack behavior, these two regimes have been explored separately as below:

4.1 Pre-crack Behavior

The original core–shell composite given in Fig. 1b with the fraction of α could get simplified to an equivalent material with the projected mechanical properties. Looking closer at the rounded arrangement of the shell around the circular core, one could discern both parallel and series arrangement in parts of the core–shell composition as depicted with the vertical and horizontal strips in the Fig. 5a.

For the vertical highlighted strip, excluding the rest of the domain, either medium would bear the entire applied force F, and the individual deformations are accumulated for the total deflection. This is known as Series behavior and any mechanical property representing strength $\square$ could get expressed versus those of the sub-volume properties of core $\square_C$ and shell $\square_S$ as:

$$\frac{1}{\square_{--}} = \frac{1-\alpha}{\square_C} + \frac{\alpha}{\square_S} \tag{6}$$

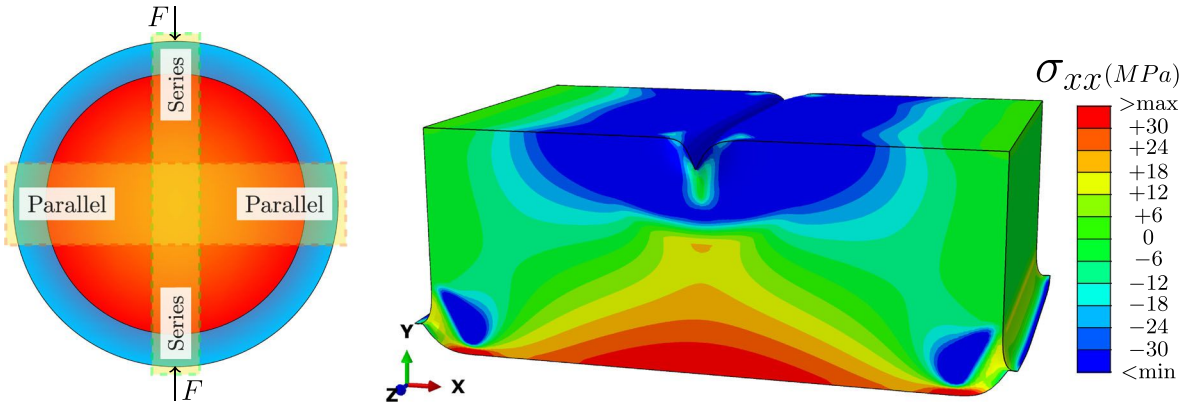

(a) The decomposition of the circular arrangement of the core and shell into more simplified parallel and series stacking modes.

(b) The distribution of the horizontal flexural stress σ_{xx} in the elastic mode, on the deformed domain, before initiation of the crack.

Fig. 5 **a** Equivalent material projection from the rounded arrangement of the core–shell composite, **b** Horizontal (tensile/compressive) stress distribution

where $\square_{--}$ is the resulted mechanical property of the series arrangement, which is smaller than either of the core and shell properties ($\square_{--} < \{\square_C, \square_S\}$). In fact, in the series arrangement, both media are fully decoupled for bearing the applied force F and they only contribute to deflection, making the composite weaker.

Respectively, for the highlighted horizontal strip, excluding the rest of the domain, either medium will bear parts of the applied force and the resulted deflections for either media would be identical. Thus, the resulted property in such parallel arrangement $\square_{\parallel}$ will be larger ($\square_{\parallel} > \{\square_C, \square_S\}$), and one has:

$$\square_{\parallel} = (1-\alpha)\,\square_C + \alpha\square_S \tag{7}$$

In fact, in parallel arrangement, both media are fully coupled for bearing the applied force F and hence they contribute to the strength. Consequently, since the entire core–shell medium of rounded geometry has two extremes mentioned above, any effective mechanical property $\square_{EFF}$ would fall in their range, as:

$$\square_{--} \leq \square_{\text{EFF}} \leq \square_{\parallel} \tag{8}$$

and one could describe the effective property $\square_{\text{EFF}}$ versus the extreme values as:

$$\square_{\text{EFF}} = f_{\parallel}\square_{\parallel} + f_{--}\square_{--} \tag{9}$$

Hence, replicating the identical core–shell geometry and testing the force–deflection behavior in ABAQUS, we have noted that the effective material properties $\square_{EFF}$ are near those of the parallel arrangement $\square_{\parallel}$ and the effect of the series arrangement is negligible. Moreover, it is obvious that in the rounded core–shell composite the level of engagement is very high and core and shell compartments are highly coupled. Hence, one can approximate $f_{\parallel} \approx 1$ and $f_{--} \approx 0$, which yields:

$$\square_{\text{EFF}} \approx \square_{\parallel} \tag{10}$$

Table 2 summarizes any of the effective mechanical properties of the equivalent material, based on those of core and shell, original given in the Table 1 for the shell fraction of $\alpha = 0.35$.

Regarding the geometry, a cube of dimensions $l = 25$ mm, $h = 10$ mm and $d = 15$ mm was created as given by the experimental condition. Two hinge line reactions were placed in the left/right bottom corners (Fig. 1a, $(x, y) = \left(\pm\frac{l}{2}, -\frac{h}{2}\right)$) which can only rotate with no vertical displacement ($\Delta y = 0$). As well, a vertical force of $F = 1500N$ was applied in the top center for the flexural test. The force magnitude was deliberately taken larger than the experimental regime since the simulation medium does not contain any inhomogeneity and defects. Subsequently, a fine mesh was created (i.e. approximate global size ≈ 0.15 mm). The simulation was carried out in 3D using C3D8R, 8-node linear brick elements for running in reduced integration mode and hourglass controls. For the mainly brittle core–shell composition, in the central location the

Table 2 Equivalent material properties for simulation ($\alpha = 0.35$)

Parameter	E_{EFF}	ν_{EFF}	G_{EFF}	$\sigma_{y,\mathrm{EFF}}$
Value	375	0.26	147	794
Unit	GPa	[]	GPa	MPa

shear stress will be zero due to symmetry ($\sigma_{xy} = 0$) and the remaining horizontal stress (i.e. σ_{xx}) on the initiated crack surface shall be the prominent drive for the progress of the cracks. Hence, it has been tracked in the elastic regime and its distribution has been illustrated in the Fig. 5b.

4.2 Post-crack Behavior

In the presence of the crack, the stress intensity factor K_I is the measure for the materials failure, defined as Soboyejo (2002):

$$K_I = \sigma\sqrt{\pi a}Y\left(\hat{a}\right) \tag{11}$$

where σ is the applied uniform stress in the vicinity of the crack, a is the crack size in the boundary, $Y\left(\hat{a}\right)$ is the shape function relating the scale of the crack to the geometry of the specimen and $\hat{a} = a/h$ is the measure for the progress of the crack length a with respect to the height of the specimen h.

There have been few approximations for the shape function Y and stress intensity factor K_I, in the flexural fracture which are presented in the Table 3, which have certain limitations that do not apply to performed experiments. As an example, Hiroshi et al. (1973) and Guinea et al. (1998) have approximated shape function $Y\left(\hat{a}\right)$ versus the original stress value in the absence of the crack, while Bower has approximated the stress intensity factor K_I for the certain geometry with the aspect ratio of $\frac{l}{h} = 4$ (Allan 2009). However, as the crack scale a grows, the remaining cross-section for bearing the load (i.e. $h - a$) gets reduced. Thus, the augmentation in the stress value is simultaneously the result of reduction in the surface area as well as the crack tip effect as a singularity. Hence, one could explore the instantaneous shape function more closely in the local scale with higher precision, which deems necessary for the specific condition of the current experiments.

While, the formation and progress of the crack during the flexural fracture has a dynamic runaway behavior in a non-equilibrium state, herein we consider a slow regime of crack growth and we treat it as a quasi-static development, and the inertial effects are neglected. In the absence of the shape function $Y\left(\hat{a}\right)$, Fig. 6a illustrates the distribution of the elastic bending stress, upon imposing the flexural load F, which causes tensile stresses in the tip of the crack of the scale of a. The crack ideally grows in a straight line in the absence of inhomogeneities. Thus, the remaining region for bearing the moment would be $h - a$ and the stress in the crack tip σ, in the absence of shape function $Y\left(\hat{a}\right)$, would be:

$$\sigma = \frac{Mc}{I} = \frac{3Fl}{b\,(h-a)^2} \tag{12}$$

Additionally, having an estimation for the local shape function Y versus the crack progress $\hat{a}$, one could estimate the critical crack size a_c, leading to the continued fracture. In this regard, a series of 2D domains have been created in plane stress condition ($\sigma_z = 0$). The initial elements were created as CPS8R 8-node biquadratic quadrilateral, for running in reduced integration mode. Subsequently, multitudes of crack sizes were assigned in the central location starting from the bottom with the Crack section using the Assign Seam tool in ABAQUS. Since the crack tip acts as a singularity, in order to increase the precision and establish computationally affordable simulation, 3 distinct zones have been created versus the distance from the crack tip with the radii of 0.25 mm and 1.25 mm. The meshing was performed from the coarser to finer scale with the approximate global size of $\approx$ 0.35 mm, $\approx$ 0.20 mm and $\approx$ 0.10 mm respectively, as shown in the Fig. 6b. As well, while most of the mesh types were created as hexagonal the mesh type in the crack tip was chosen as triangular, which matches with the crack geometry. Subsequently, a flexural compressive load $F = 100\,\mathrm{N\,mm^{-1}}$ (equivalent to $F = 1500N$ in earlier $3D$ simulation) was exerted in the top center. Finally, the finite element method solved the cluster of equations numerically, with final convergence. In the post-processing, the maximum horizontal stress $\sigma_{\max}$,

Table 3 Values for the shape function $Y(\hat{a})$ and the stress intensity factor K_I from the literature

Parameter	Relationship	References
$Y(\hat{a})$	$\frac{1}{\sqrt{\pi}} \cdot \frac{1.99 - \hat{a}(1-\hat{a})\left(2.15 - 3.93\hat{a} + 2.7\hat{a}^2\right)}{(1+2\hat{a})(1-2\hat{a})^{3/2}}$	Hiroshi et al. (1973)
$Y(\hat{a})$	$\frac{\sqrt{\hat{a}}}{(1-\hat{a})^{3/2}(1+3\hat{a})}\left\{p_\infty(\hat{a}) + \frac{4}{\beta}\left(p_4(\hat{a}) - p_\infty(\hat{a})\right)\right\}$	Guinea et al. (1998)
K_I	$\frac{4P}{B}\sqrt{\frac{\pi}{h}}\left(1.6\hat{a}^{1/2} - 2.6\hat{a}^{3/2} + 12.3\hat{a}^{5/2} - 21.2\hat{a}^{7/2} + 21.8\hat{a}^{9/2}\right)$	Allan (2009)

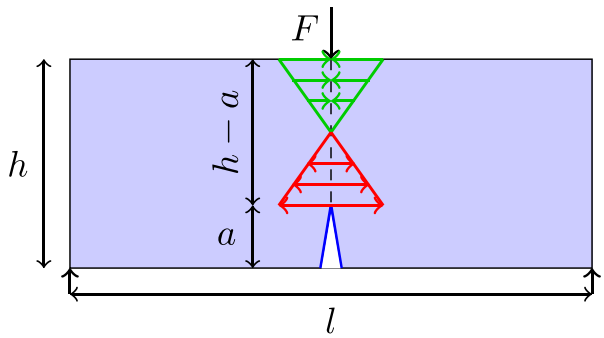

(a) The generated horizontal elastic stress σ_{xx} on the remaining real-estate $(h-a)$ for bearing the flexural load, excluding the effect of shape function $Y(\hat{a})$; red: tension, green: compression.

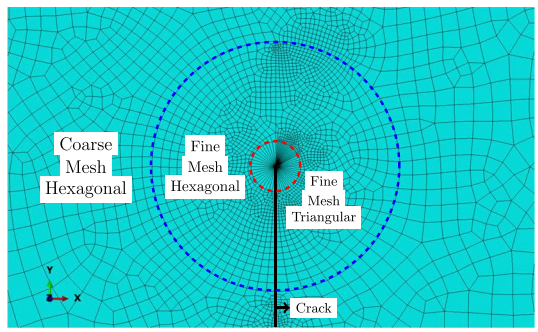

(b) The mesh distribution map, in 3 distinct zones of small gradients (coarse), larger gradients (fine) largest gradient in the crack tip singularity (finest scale).

Fig. 6 **a** The elastic stress excluding the shape function, **b** meshing pattern around the crack and beyond

which occurs at the crack tip, and the maximum vertical deflection $\delta_{\max}$ (i.e. occurring at the top center) were extracted. Figure 7a illustrates the distribution of the horizontal stress σ_{xx} at the 3 quartiles of the crack progress (i.e. $\hat{a} = \left\{\frac{1}{4}, \frac{1}{2}, \frac{3}{4}\right\}$).

The shape factor, in fact, is a multiplier (i.e. coefficient) for the generated stress in the crack tip, as a type of stress concentration factor, and could be calculated versus either the instantaneous flexural stress σ(True shape function Y_{True}) or the original applied flexural stress σ_0 (Engineering shape function Y_{Eng}) as:

$$Y = \begin{cases} \frac{\sigma_{\max}}{\sigma} & \text{True} \\ \frac{\sigma_{\max}}{\sigma_0} & \text{Engineering} \end{cases} \tag{13}$$

Both Engineering $Y_{\text{Eng.}}$and True Y_{True} shape functions have been visualized in the Fig. 7b, with their second order polynomial interpolations as:

$$\begin{cases} Y_{\text{True}} = 2.2 - 4.1\hat{a} + 2.8\hat{a}^2 \\ Y_{\text{Eng}} = 2.1 - 9.2\hat{a} + 16.8\hat{a}^2 \end{cases} \tag{14}$$

Needless to mention that, the instigation of the cracks occurs from the cavities/impurities as singularity points, and since the assigned simulation domain is perfectly uniform, the progress of the crack has been assigned manually for the continued fracture. Other than the crack tip as the cohesive zone, the stress values in the rest of the domain are less than the projected effective yield value $\sigma_{y,\text{EFF}}$ (Table 2) as shown in the pre-crack (Fig. 5b) and post-crack (Fig. 7a) regimes of simulations to ensure that the material does not solely fail to excessive loading.

5 Results and Discussions

Looking closer at the pattern of the flexural deflection, one could divide it to the 3 stages of the initiation, pre-crack deflection, and post-crack deflection, where the crack forms and grows in size from smaller to larger scales. Having the stiffness K as a measure for the strength, the initial stiffness before the formation of the

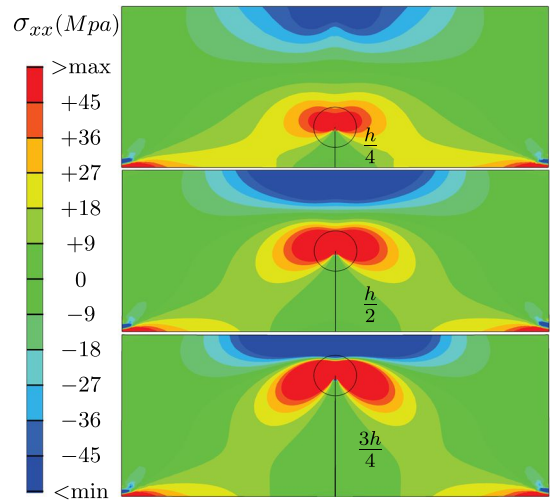

(a) The distribution of the normal horizontal stress σ_{xx} in the first, second and third quartiles of the crack progress ($\hat{a} = \left\{\frac{1}{4}, \frac{1}{2}, \frac{3}{4}\right\}$) shown on the original undeformed domain.

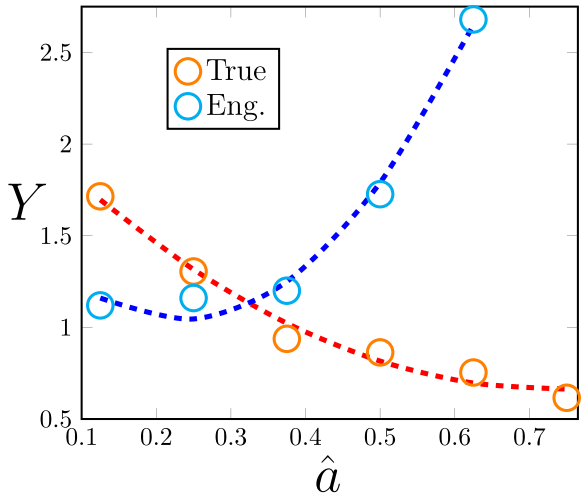

(b) The obtained shape function Y versus the crack progress $\hat{a}$, which is calculated versus the original (engineering) pre-crack stress σ_0 as well as the instantaneous (true) maximum stress σ.

Fig. 7 **a** The allocation of horizontal stress σ_{xx} versus the crack progress, **b** computed shape functions versus the original and instantaneous stress state

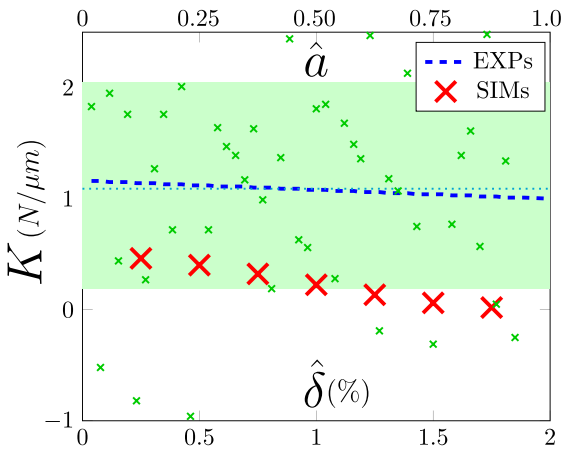

Fig. 8 The comparison of the pre-crack experimental stiffness K_{EXP} (small cracks only) versus the normalized deflection $\hat{\delta}$ with the obtained post-crack simulation stiffness K_{SIM} (large opening in the center) versus the crack progress $\hat{a}$

cracks could get approximated via the theoretical calculation in flexural test as $K_{\text{THE}} \approx \frac{48 E_{\text{EFF}} I}{l^3} \approx 11 \frac{N}{\mu\text{m}}$. The middle stages of the flexural loading in the presence of small cracks (and absence of the large crack in the middle), can be approximated via the experimental measurements. In this regard, Fig. 8 tracks the instantaneous stiffness during the experiment where the average value is obtained as $K_{\text{EXP}} \approx 1.1 \frac{N}{\mu\text{m}}$. Finally, the simulations stiffness is obtained in the presence of the main large crack in the center, which is shown in this Figure versus the crack progress measure $\hat{a}$, and the obtained stiffness is averaged at $K_{\text{SIM}} \approx 0.27 \frac{N}{\mu\text{m}}$. Hence, the obtained correlation is:

$$K_{\text{THE}} > K_{\text{EXP}} > K_{\text{SIM}} \tag{15}$$

which is valid comparison since throughout the flexural test the small cracks form, and the stiffness should get reduced from the initial stage (K_{THE}), passing through the pre-crack middle stages with only small cracks (K_{EXP}) and finally forming the post-crack large opening in the middle (K_{SIM}).

From the obtained relationship for the stress intensity K_I and the interpolated true shape function $Y_{\text{True}}(\hat{a})$ for the flexural test, one could estimate the critical crack size a_c, where fracture occurs/propagates. Therefore having the K_{IC} as the critical stress intensity factor one has:

$$\frac{3Fl\sqrt{\pi a}}{d\,(h-a)^2}\left(2.1 - 9.2\frac{a}{h} + 16.8\left(\frac{a}{h}\right)^2\right) := K_{IC} \tag{16}$$

which algebraically gets simplified into:

$$Q_5\lambda^5 + Q_4\lambda^4 + Q_3\lambda^3 + Q_2\lambda^2 + Q_1\lambda + Q_0 = 0 \tag{17}$$

where $\lambda = \sqrt{a}$ and the coefficients Q_5 to Q_1 for the polynomial are extracted as:

$$Q_5 = 50.4C \quad , Q_4 = h^2 \quad , Q_3 = -27.6Ch,$$
$$Q_2 = -2h^3 \quad , Q_1 = 6.3Ch^2 \quad , Q_0 = -h^4$$

where $C = \dfrac{Fl\sqrt{\pi}}{dK_{IC}}$ is a constant representing the ratio of the applied external force F to the internal fracture resistance K_{IC} as well as the length to depth aspect ratio l/d. For estimating the range of the critical crack length a_c, since it is a very small number, one could neglect the higher order terms of $\sqrt{a}$ since $\lambda \gg \lambda^2 \gg \ldots$, and linearization of the Eq. (17) leads to:

$$a_c \sim \left(\frac{h^2 dK_{IC}}{6.3Fl\sqrt{\pi}}\right)^2 \tag{18}$$

using the geometric dimensions given in the Table 1 and noting the fracture toughness of tantalum carbide TaC as 6.63MPa$\sqrt{m}$ (Song et al. 2016) and the force magnitude of $F = 1500N$ from the simulations, the critical crack length a_c for the fracture is obtained as:

$$a_c <\sim 0.5\text{mm} \tag{19}$$

The inequality is due to the fact that for the assumed perfect material, the inhomogeneities and defects are not considered. In fact, it is the most optimistic case scenario and the critical crack length for the fracture could be lower. As well, while the instantaneous opening can occur in this scale the subsequent larger scale response could be assessed from the slope of the $F-\delta$ diagram. In fact, the larger-scale response could mostly depend on the existence of the real-time imperfections or heterogenous material composition in the crack tip, such as laminates.

The role of the stacking mode (Parallel vs Perpendicular) on the failure can be studied from the energy perspective. In this regard, the applied total external energy E_{TOT} can be calculated, as:

$$E_{\text{TOT}} = \int F d\delta \tag{20}$$

where F is applied external force and $d\delta$ is the resulted infinitesimal displacement. Such energy is either stored in the deflecting block elastically E_{EL} (which could retain back to the original shape with springy behavior), or lead to fracture E_{FR} and generate surfaces of the cracks. Hence:

$$E_{\text{TOT}} = E_{\text{EL}} + E_{\text{FR}} \tag{21}$$

In principle, the purpose of coating the TaC core material with the shell (i.e. Graphite) is to impel the cracks to propagate within the shell material rather than the core so that the composite material can endure more and resist fracture. In this way, the shell layer acts as a shock absorber which softens the composite material. In this regard, since the perpendicular arrangement (0–90) has more stress concentration due to point contacts between the orthogonal cylindrical composites, it tends to generate more cracks ($E_{FR} \uparrow$) which locally relaxed the medium ($E_{EL} \downarrow$), and allows endurance before the next local crack. This is obvious in Fig. 9a where the distance of the failure zones is relatively higher than those of the parallel arrangements shown in Fig. 9b. Another way of explaining the two-stage failure peaks would be the initial graphite (i.e. shell) fracture followed by the secondary TaC (i.e. core) fracture later on.

A measure for the crack deflection could be the number of kinks along its propagation pathway, which infers the change in the direction of the propagation. Such twisted move increases the tortuosity τ. Thus, the tortuosity τ could be an indicative measure for the crack deflection. In this regard, since the outer graphite is more disintegrated and absorbs some fraction of the energy along the way, the remainder energy E_{EL} will be smaller and tend to make more straight pathway ($\tau \downarrow$). Therefore, the higher graphite fraction α, forms more straight cracks with crack arrest, while more core fraction accumulates larger elastic energy for release and generates more tortuous cracks. Hence:

$$\alpha \uparrow \sim \tau \downarrow \tag{22}$$

Such relationship could additionally be verified from the perspective of the strength. Obviously, the propagation pathway of the crack could either be from inside the blocks (i.e more straight) or their periphery (i.e. more tortuous), and since the larger shell fraction $\alpha \uparrow$ makes the block weaker it provides more possibility for the cracks to propagate in the straight route (i.e. $\tau \downarrow$) and one gets the following relationship:

$$\tau_{\text{No Collapse}} > \tau_{\text{Shell Collapse}} > \tau_{\text{Core Collapse}} \tag{23}$$

Figure 10 shows that the values of the computed tortuosity from the averaged Left-Right periphery (LR)

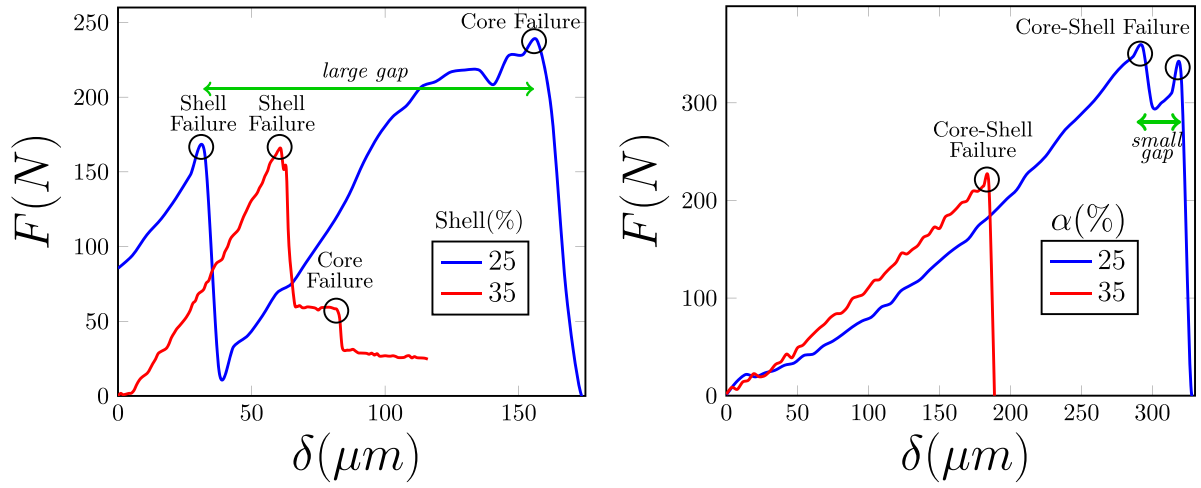

(a) Perpendicular arrangement $(0-90)$. (b) Parallel arrangement $(0-0)$.

Fig. 9 The force-displacement diagrams for two stacking configurations (0–0) vs (0–90) versus their respective graphite shell content $\alpha\%$

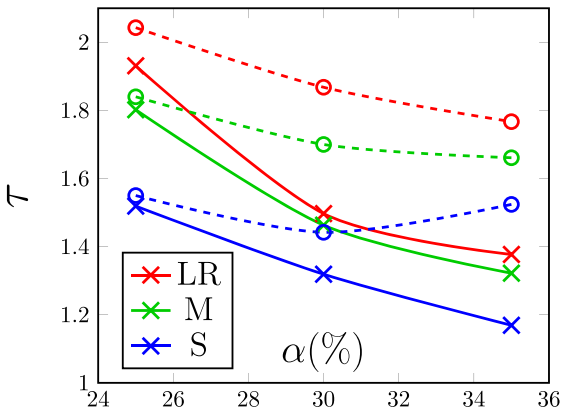

Fig. 10 Tortuosity variation versus the graphite content ($\alpha\%$) as well as the stacking mode (solid: Parallel (0–0), dashed: Perpendicular (0–90))

method is greater than the values of the other two methods in the two fibers arrangements (0–0 and 0–90). As well, one can notice that the values of the Mid-section pathway (M) method are slightly close to that of the (LR) method. This is because the (LR) method follows the exact path on the periphery, considering the crack branching whereas the mid-section method (M) considers the instantaneous center from the left and right borders which could get be neutralized. On the other hand, Dijkstra's shortest path method (S), considers the most straight pathway possible (Fig. 4c). Hence, (LR) is the most accurate among the three methods since it captures the local twisted-ness, which includes the branch information.

The other obvious trend in Fig. 10 is the larger tortuosity in the perpendicular arrangement than the parallel version. This could be due to the existence of higher variety of pathways in the perpendicular (0–90) arrangement versus the parallel (0–0) which tends to have more uniform medium; therefore:

$$\tau_{0\text{-}90} > \tau_{0-0} \tag{24}$$

The energy of the fracture E_{FR}, which is a part of the applied total energy E_{TOT} is spent on generating new surfaces which initiate on the crack tip (Le et al. 2013). This is accompanied by the release of the elastic energy where the load F drops considerably. The fracture energy E_{FR} could get divided to generate the main body cracks E_{Main}, or their branches E_{Branch}, as:

$$E_{\text{FR}} = E_{\text{Main}} + E_{\text{Branch}} \tag{25}$$

Additionally, the correlation of the applied total energy E_{TOT} to the tortuosity of the cracks becomes the most obvious, when a large fraction of it is spent for the fracture energy E_{FR} and the formation of the tortuous cracks (i.e. τ). Such crack promotion is in fact the most obvious in the 0–90 stacking forms macro-cracks within the bi-directional arrangement, the composites are less packed than in the unidirectional arrangement and there are free spaces remaining between the subsequent layers after the cold and hot pressing, Vahideh et al. (2019). As well, the existence of the graphite fiber

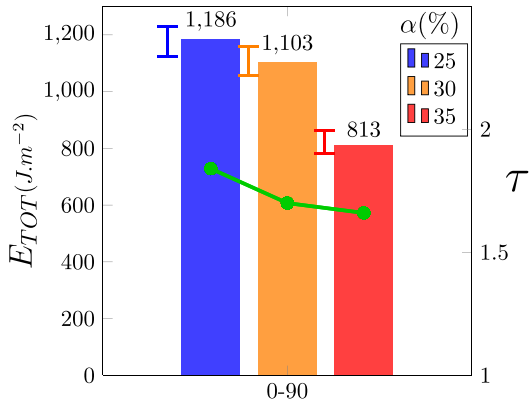

(a) The applied energy E_{TOT} for the samples, compared with the generated tortuosity τ from the averaging left/right crack boundaries (LR) method, in the perpendicular stacking. .

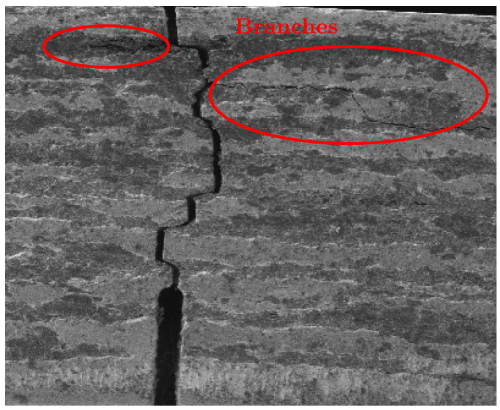

(b) Example showing the mis-correlation between the applied energy E_{TOT} the obtained tortuosity $\tau$from the shortest path (S) and mid-section (M) method which do not account for the side branches while the left/right boundary averaging (LR) considers the them in and yields a higher precision.

Fig. 11 **a** Correlation of the applied energy E_{TOT} with the obtained tortuosity $\tau$from averaging left/right crack boundaries (LR) method. **b** Example showing the the higher precision for averaging left/right crack boundaries method (LR) with respect to the shortest path (S) and mid-section (M) methods

fraction α forms local micro-cracks since the graphite has a less-packed structure, leading to a bigger chance for extending to the larger cracks, which promotes cracking (Kovar et al. 1997). Such direct correlation is visualized in Fig. 11a. Figure 11b illustrates that while the branches are generated by the applied energy E_{TOT}, the shortest path (S) and mid-section (M) methods can not capture them, since they tend to move along the straight line from the top to the bottom, while averaging left/right crack boundary (LR) walks along the generated surface and could capture more accurate tortuosity for the cracks to resonate with the applied energy E_{TOT}.

Needless to mention that the developed percolation-based method for tortuosity in this work is crack geometry-based and therefore it could broadly be applied to any fractured environment in a given material composition.

6 Conclusions

In this paper, a percolation-based framework is devised for quantifying the tortuosity τ of the fractured region, as a measure for the crack deflection, formed during 3-point flexural loading of the stacked core–shell composites, which consist of co-extruded billets of tantalum carbide TaC and graphite Gr as core and shell compartments respectively. In this regard, the peripheral region and inner area of the of the generated cracks are quantified via percolation through the 1st order neighbors and their tortuosity τ is computed via establishing three distinct methods of shortest path (S), mid-section (M) and averaging left/right crack boundaries (LR). The fracture energy (E_{FR}) and crack tortuosity (τ) have been correlated versus the variations in the shell fraction α and the stacking mode (0–0, 0–90), the role of (sub)branches the as underlying reasons for higher precision in the LR method has been addressed. The higher ductility and fracture toughness in the parallel stacking have been attributed to increased contact between layers, whereas the early failure of the perpendicular stacking (0–90) was accredited to stress concentration between the orthogonal billets.

On the other hand, a series of simulations have been performed versus the stages of the crack progress. In this regard, the equivalent material properties have been established and the obtained the stress augmentation in the crack tip leads to a simplified formulation for the true (real-time) and engineering shape function Y. Subsequently, the critical crack size a_c for the instantaneous fracture is attained versus the applied flexural load, the fracture toughness and the geometry of the bending

medium. This study could pave the way for quantifying the efficacy of the crack deflection based on the tortuosity computation and optimization of composition/stacking to achieve the desired fracture resistance.

Acknowledgements The authors would like to acknowledge Fadi Elias from American University of Beirut for the earlier partial help on the providing the data and Prof. William A. Goddard III from California Institute of Technology for the initial meeting.

Author contributions A.A: Conceptualization, Validation, Formal Analysis, Investigation, Data Curation, Writing Original Draft, Writing—Review/Editing, Visualization M.K.: Data Curation, Simulations N. V., V. S., M. K.: Methodology, Supervision, Project Administration.

Data availibility No datasets were generated or analysed during the current study.

Declarations

Competing interests The authors declare no competing interests.

References

Adharapurapu RR, Vecchio KS, Jiang F, Rohatgi A (2005) Effects of ductile laminate thickness, volume fraction, and orientation on fatigue-crack propagation in ti-al 3 ti metal-intermetallic laminate composites. Metall Mater Trans A 36(6):1595–1608

Artina M, Fornasier M, Micheletti S, Perotto S (2015) Anisotropic mesh adaptation for crack detection in brittle materials. SIAM J Sci Comput 37(4):B633–B659

Aryanfar A, Goddard W III, Marian J (2019) Constriction percolation model for coupled diffusion-reaction corrosion of zirconium in pwr. Corros Sci 158:108058

Asghar A, Hoffmann MR, Goddard WA III (2019) Finite-pulse waves for efficient suppression of evolving mesoscale dendrites in rechargeable batteries. Phys Rev E 100(4):042801

Bai Y, Sun M, Li M, Fan S, Cheng L (2018) Improved fracture toughness of laminated zrb2-sic-mosi2 ceramics using sic whisker. Ceram Int 44(8):8890–8897

Bai Y, Ma Y, Sun M, Fan S, Cheng L (2019) Strong and tough zrb2 materials using a heterogeneous ceramic-metal layered architecture. J Am Ceram Soc 102(9):5013–5019

Baskaran S, Halloran JW (1993) Fibrous monolithic ceramics: II, flexural strength and fracture behavior of the silicon carbide/graphite system. J Am Ceram Soc 76(9):2217–2224

Bermejo R, Danzer R (2010) High failure resistance layered ceramics using crack bifurcation and interface delamination as reinforcement mechanisms. Eng Fract Mech 77(11):2126–2135

Bezenšek B(2003) Elastic-plastic crack problems in the ductile-brittle transition. PhD thesis, University of Glasgow

Black JT, Kohser RA (2020) DeGarmo's materials and processes in manufacturing. Wiley, Hoboken

Boccaccini AR, Atiq S, Boccaccini DN, Dlouhy I, Kaya C (2005) Fracture behaviour of mullite fibre reinforced-mullite matrix composites under quasi-static and ballistic impact loading. Compos Sci Technol 65(2):325–333

Bower AF (2009) Applied mechanics of solids. CRC Press, Boca Raton

Bower AF, Ortiz M (1991) A three-dimensional analysis of crack trapping and bridging by tough particles. J Mech Phys Solids 39(6):815–858

Bower AF, Ortiz M (1993) The influence of grain size on the toughness of monolithic ceramics

Bueno S, Baudín C (2009) Design and processing of a ceramic laminate with high toughness and strong interfaces. Composites Part A 40(2):137–143

Clegg WJ, Howard SJ, Lee W, Phillipps AJ, Stewart RA (1994) Interfacial cracking in ceramic laminates. Compos Interfaces 2(5):337–349

Davis JB, Kristoffersson A, Carlström E, Clegg WJ (2000) Fabrication and crack deflection in ceramic laminates with porous interlayers. J Am Ceram Soc 83(10):2369–2374

Deng Y, Li W, Shao J, Zhang X, Kou H, Geng P, Zhang X, Li Y, Ma J (2017) A novel theoretical model to predict the temperature-dependent fracture strength of ceramic materials. J Eur Ceram Soc 37(15):5071–5077

Dijkstra EW et al (1959) A note on two problems in connexion with graphs. Numer Math 1(1):269–271

Dusane AR, Budarapu PR, Pradhan AK, Natarajan S, Reinoso J, Paggi M (2022) Simulation of bridging mechanisms in complex laminates using a hybrid pf-czm method. Mech Adv Mater Struct 29(28):7743–7771

Entezari A, Roohani-Esfahani S-I, Zhang Z, Zreiqat H, Dunstan CR, Li Q (2016) Fracture behaviors of ceramic tissue scaffolds for load bearing applications. Sci Rep 6(1):1–10

Fabbrocino F, Funari MF, Greco F, Lonetti P, Luciano R, Penna R (2019) Dynamic crack growth based on moving mesh method. Composites Part B 174:107053

Faber KT, Evans AG (1983) Crack deflection processes-i. Theory. Acta Metall 31(4):565–576

Fahrenholtz WG, Wuchina EJ, Lee WE, Zhou Y (2014) Ultra-high temperature ceramics: materials for extreme environment applications. Wiley, Hoboken

Guinea GV, Pastor JY, Planas J, Elices M (1998) Stress intensity factor, compliance and cmod for a general three-point-bend beam. Int J Fract 89:103–116

Hefter J, Arlene Hecker F, Mahoney M, Harris JE (1993) Microstructural characterization of structural ceramics using image processing and analysis. J Am Ceram Soc 76(6):1551–1557

Heimann RB (2010) Classic and advanced ceramics: from fundamentals to applications. Wiley, Hoboken

Hilmas G, Brady A, Abdali U, Zywicki G, Halloran J (1995) Fibrous monoliths: non-brittle fracture from powder-processed ceramics. Mater Sci Eng A 195:263–268

Hossain MZ, Hsueh C-J, Bourdin B, Bhattacharya K (2014) Effective toughness of heterogeneous media. J Mech Phys Solids 71:15–32

Hvizdoš P, Tatarko P, Duszova A, Dusza J (2013) Failure mechanisms of ceramic nanocomposites. In: Ceramic nanocomposites. Elsevier, Amsterdam, pp 117–152

Hwang JH, Lee CS, Hwang W (2001) Effect of crack propagation directions on the interlaminar fracture toughness

of carbon/epoxy composite materials. Appl Compos Mater 8(6):411–433
Inoue J, Nambu S, Ishimoto Y, Koseki T (2008) Fracture elongation of brittle/ductile multilayered steel composites with a strong interface. Scripta Mater 59(10):1055–1058
Jayaram MA, Fleyeh H (2016) Convex hulls in image processing: a scoping review. Am J Intell Syst 6(2):48–58
Khan R (2019) Fiber bridging in composite laminates: a literature review. Compos Struct 229:111418
Kovar D, King BH, Trice RW, Halloran JW (1997) Fibrous monolithic ceramics. J Am Ceram Soc 80(10):2471–2487
Le Yu, Liu H, Wang Y, Kuwata N, Osawa M, Kawamura J, Ye S (2013) Preferential adsorption of solvents on the cathode surface of lithium ion batteries. Angew Chem 125(22):5865–5868
Lee WK, Ratnam MM, Ahmad ZA (2016) Detection of fracture in ceramic cutting tools from workpiece profile signature using image processing and fast fourier transform. Precis Eng 44:131–142
Li Y, Zhou M (2013) Prediction of fracturess toughness of ceramic composites as function of microstructure Ii analytical model. J Mech Phys Solids 61(2):489–503
Li X, Zou L, Ni H, Reynolds AP, Wang C, Huang Y (2008) Micro/nanoscale mechanical characterization and in situ observation of cracking of laminated si3n4/bn composites. Mater Sci Eng C 28(8):1501–1508
Linstrom PJ, Mallard WG (2001) The nist chemistry webbook: a chemical data resource on the internet. J Chem Eng Data 46(5):1059–1063
Liu H, Hsu SM (1996) Fracture behavior of multilayer silicon nitride/boron nitride ceramics. J Am Ceram Soc 79(9):2452–2457
Liu Y, Li B, Chongjun W, Zheng Y (2016) Simulation-based evaluation of surface micro-cracks and fracture toughness in high-speed grinding of silicon carbide ceramics. Int J Adv Manuf Technol 86(1):799–808
Luna GG, Axinte D, Novovic D (2020) Influence of grit geometry and fibre orientation on the abrasive material removal mechanisms of SiC/SiC ceramic matrix composites (CMCS). Int J Mach Tools Manuf 157:103580
Moattari M, Sattari-Far I, Persechino I, Bonora N (2016) Prediction of fracture toughness in ductile-to-brittle transition region using combined CDM and Beremin models. Mater Sci Eng A 657:161–172
Mosler J, Meschke G (2004) Embedded crack vs. smeared crack models a comparison of elementwise discontinuous crack path approaches with emphasis on mesh bias. Comput Methods Appl Mech Eng 193(30–32):3351–3375
Muju S (2000) Crack propogation in bimaterial multilayered periodically microcracking composite media. Compos Sci Technol 60(12–13):2213–2221
Needleman A, Tvergaard V (1994) Mesh effects in the analysis of dynamic ductile crack growth. Eng Fract Mech 47(1):75–91
Nino A, Hirabara T, Sugiyama S, Taimatsu H (2015) Preparation and characterization of tantalum carbide (tac) ceramics. Int J Refract Metal Hard Mater 52:203–208
Oechsner M, Hillman C, Lange FF (1996) Crack bifurcation in laminar ceramic composites. J Am Ceram Soc 79(7):1834–1838
Otsu N (1975) A threshold selection method from gray-level histograms. Automatica 11(285–296):23–27
Parmigiani JP, Thouless MD (2006) The roles of toughness and cohesive strength on crack deflection at interfaces. J Mech Phys Solids 54(2):266–287
Peng J, Dong H, Hojamberdiev M, Yi D, Yang Y, Bao H, Li H, Li H, Mao D, Meng L (2017) Improving the mechanical properties of tantalum carbide particle-reinforced iron-based composite by varying the tac contents. J Alloy Compd 726:896–905
Perrière L, Valle R, Mazerolles L, Parlier M (2008) Crack propagation in directionally solidified eutectic ceramics. J Eur Ceram Soc 28(12):2337–2343
Phillipps AJ, Clegg WJ, Clyne TW (1993) Fracture behaviour of ceramic laminates in bending-i modelling of crack propagation. Acta Metall Mater 41(3):805–817
Qiu M, Finlayson GD, Qiu G (2008) Contrast maximizing and brightness preserving color to grayscale image conversion. In: Conference on colour in graphics, imaging, and vision. Society for Imaging Science and Technology, pp 347–351
Rezaei F, Kakroudi MG, Shahedifar V, Vafa NP, Golrokhsari M (2017) Densification, microstructure and mechanical properties of hot pressed tantalum carbide. Ceram Int 43(4):3489–3494
Sarah K, Thamburaja P, Srinivasa A, Reddy JN (2020) Numerical simulations of damage and fracture in viscoelastic solids using a nonlocal fracture criterion. Mech Adv Mater Struct 27(13):1085–1097
Shahedifar V, Kakroudi MG (2018) Fracture behavior improvement of tac-based ceramic composites by fibrous structure. Int J Refract Metals Hard Mater 71:15–20
Shahedifar V, Kakroudi MG, Baharvandi HR, Rezaei F (2019) Investigation of strength, fracture toughness, and crack propagation pattern of tac-based fibrous monoliths as a function of microstructure architecture. Int J Refract Metals Hard Mater 78:332–339
Shahedifar V, Kakroudi MG, Vafa NP (2020) Characterization of tac-based fibrous-monolithic ceramics made of fibers with different core/shell volume ratios and orientations. Mater Sci Eng A 775:138935
Silvestroni L, Pienti L, Guicciardi S, Sciti D (2015) Strength and toughness: the challenging case of tac-based composites. Composites Part B 72:10–20
Skiena S (1990) Dijkstra's Algorithm. Implementing Discrete Mathematics: Combinatorics and Graph Theory with Mathematica. Addison-Wesley, Reading, pp 225–227
Soboyejo W (2002) Mechanical properties of engineered materials. CRC Press, Boca Raton
Song K, Yunhua X, Zhao N, Zhong L, Shang Z, Shen L, Wang J (2016) Evaluation of fracture toughness of tantalum carbide ceramic layer: a vickers indentation method. J Mater Eng Perform 25:3057–3064
Tada H, Paris PC, Irwin GR (1973) The stress analysis of cracks. Handbook, Del Research Corporation, 34(1973)
Tallinen T, Mahadevan L (2011) Forced tearing of ductile and brittle thin sheets. Phys Rev Lett 107(24):245502
Thamburaja P, Sarah K, Srinivasa A, Reddy JN (2019) Fracture of viscoelastic materials: Fem implementation of a non-local & rate form-based finite-deformation constitutive theory. Comput Methods Appl Mech Eng 354:871–903
Torre LL, Winkler B, Schreuer J, Knorr K, Avalos-Borja M (2005) Elastic properties of tantalum carbide (tac). Solid State Commun 134(4):245–250

Valerio Carollo J, Reinoso MP (2018) Modeling complex crack paths in ceramic laminates: a novel variational framework combining the phase field method of fracture and the cohesive zone model. J Eur Ceram Soc 38(8):2994–3003

Vandenberghe N, Villermaux E (2013) Geometry and fragmentation of soft brittle impacted bodies. Soft Matter 9(34):8162–8176

Warwick CM, Clegg WJ (2009) Crack deflection at structured interlayers. In: Proceedings of composites, advanced ceramics, materials, and structures-B-19 Conference, p 847

Watts J, Hilmas G (2006) Crack deflection in tungsten carbide based laminates. Int J Refract Metal Hard Mater 24(3):222–228

Wei C, Zhang X, Li S (2014) Laminated zrb2-sic/graphite ceramics with simultaneously improved flexural strength and fracture toughness. Ceram Int 40(3):5001–5006

Wei C, Chenglin W, Wojnar C (2019) Effect of patterned inclusions on the fracture behavior of ceramic composites. Composites Part B 172:564–592

Yasmin A, Daniel IM (2004) Mechanical and thermal properties of graphite platelet epoxy composites. Polymer 45(24):8211–8219

Zhou F, Molinari J-F (2004) Dynamic crack propagation with cohesive elements: a methodology to address mesh dependency. Int J Numer Methods Eng 59(1):1–24

Zou L, Huang Y, Chen R, Wang CA, Park D-S (2003) The measurement and characterization of the interfacial toughness of si3n4/bn composites by a three-point bending test. J Eur Ceram Soc 23(11):1987–1996